



TECHNICAL ARTICLE

Structure-Dependent Corrosion Behavior of Electrodeposited Zn Coating

Harikrishna Kancharla, G.K. Mandal, H.S. Maharana, S.S. Singh, and K. Mondal

Submitted: 19 March 2022 / Revised: 17 May 2022 / Accepted: 20 July 2022 / Published online: 14 September 2022

In the present work, zinc (Zn) coating was developed on an interstitial-free (IF) steel from Zn sulfate bath using direct current (DC) and pulse current (PC) electrodeposition techniques at different current densities of 10, 30, and 60 mA/cm². The x-ray diffraction (XRD) analysis of the coatings reveals that the higher atomically dense (0002) crystal plane of the pure Zn in the PC deposits is pronounced as compared to the DC deposits. The scanning electron microscopic (SEM) study displays finer and compact morphology of the PC deposits as compared to the DC deposits. The electrodeposits change from coarser to finer morphology with an increase in current density in both the electrodeposition techniques. All the PC deposits show a higher water contact angle (WCA) as compared to the DC deposits at each applied current density. The finer and compact coating morphology, higher WCA values with the dominance of a higher atomically dense (0002) crystal plane as well as the higher fraction of simonkolleite phase lead to the higher corrosion resistance of the PC deposits than the DC deposits.

Keywords corrosion, electrodeposition, wettability, Zn coating

1. Introduction

Zinc is widely used as a sacrificial anodic coating on ferrous components for corrosion protection. Moreover, Zn coating acts as a sacrificial anode and provides cathodic protection to the steel (Ref 1, 2). Zn-coated steel products are employed in a wide range of applications, such as the automobile industry, harbor facilities, outdoor exposition, transmission power lines, and construction sectors (Ref 1). Most of the commercially available Zn-coated steels are produced by traditional coating technologies, such as hot-dip galvanization, spraying, and thermal process (Ref 1, 2). However, they have their own limitations. For example, the hot-dip galvanization process is applicable for large-scale production. However, it is not suitable for small-sized parts due to higher production costs and limitations to obtain reduced coating thickness for relatively non-corrosive applications. Moreover, the hot-dip galvanization process requires a high processing temperature and expensive equipment to produce Zn coatings (Ref 3). In addition, the commercially produced Zn coatings are smooth, soft, and have a greater tendency to mechanical damage (Ref 1, 2). Therefore, easy-to-produce coatings with novel coating structure and morphology are required to improve the physical, chemical, mechanical, and electrochemical properties. Among

all the coating technologies, electrodeposition is one of the most economic and environmentally friendly processes for producing thinner metallic coatings for various applications (Ref 3-5). Moreover, the electrodeposition process can easily produce the desired coatings at room temperature (Ref 3-5).

Electrodeposited coatings are mostly used in small- and medium-sized applications, such as nuts, bolts, bicycles, and automobile body parts. In recent years, direct current (DC) and pulse current (PC) electrodeposition techniques are widely recognized for their effectivity in making better coating quality and performance in various applications (Ref 3-5). In addition, continuous electroplating process is also available for producing Zn-coated steel sheets with excellent surface finish, making this product ideal for application in exterior body panels of automobiles (Ref 1-5). In general, heavier electrodeposited Zn coatings are predominantly used for automobile body parts, whereas thinner electroplated coatings are preferred for indoor applications, where corrosion atmosphere is not acute (Ref 1, 5).

Assaf et al. (Ref 6) have documented the effect of electrodeposition parameters, such as current density, bath composition, temperature, and pH, on the electrodeposition of Zn on the steel substrate. They have suggested that the electrodeposited Zn coatings prepared at lower current densities ($< 3 \text{ mA/cm}^2$) and concentration of Zn ions ($< 5 \text{ g/dm}^3$) affect the coating morphologies and surface defects due to insufficient cathodic current efficiency for Zn deposition. Similarly, Chen et al. (Ref 7) have studied that the PC deposition process is better for improving the properties of the electrodeposited coating due to its higher instantaneous current density than the DC deposition process. They have also suggested that the practical current limit for the PC could be much higher than the DC deposition. Some of the studies have also documented that the PC deposition provides a smooth and compact coating with less porosity and better mechanical properties, such as hardness as well as ductility (Ref 8). Al-Dhire et al. (Ref 9) have also reported that the PC deposition facilitates the fineness of the

Harikrishna Kancharla, S.S. Singh, and K. Mondal, Department of Materials Science and Engineering, Indian Institute of Technology, Kanpur, UP 208016, India; **G.K. Mandal**, CSIR-National Metallurgical Laboratory, Jamshedpur, Jharkhand 831009, India; and **H.S. Maharana**, Central Glass and Ceramic Research Institute, Kolkata, West Bengal 700032, India. Contact e-mail: kallol@iitk.ac.in.

coating structure and results in better corrosion resistance as compared to the coatings produced by the DC deposition. They have also suggested that grain refinement occurs during the PC due to the higher nucleation rate on the substrate surface.

Moreover, the corrosion properties of Zn coatings not only depend on process parameters, but also on the texture (crystallographic orientation) of the coating. Scully et al. (Ref 10) have demonstrated that the orientation of the Zn coating related to the (0002) crystal plane shows higher corrosion resistance than other crystallographic orientations. They have also suggested that the (0002) crystal planes have a higher binding energy of the surface atoms (closed packed plane), resulting in higher resistance to dissolution. However, the reported studies have not elaborated on the effect of applied current densities on the texture and corrosion behavior of Zn electrodeposits obtained from Zn sulfate bath by the PC and DC deposition techniques.

Nowadays, hydrophobicity on the metal surface has attracted a lot of attention due to its anti-corrosion, anti-fouling, and self-cleaning applications (Ref 11-13). The hydrophobic properties of the solid surfaces are influenced by surface morphology and geometric structure of the surface. The water contact angle (WCA) between the water droplet and surface greater than 90° is commonly called hydrophobic surface (Ref 11-13). Creating the hydrophobic surface on the metal surfaces can be done in two ways: creating a rough structure and another modifying a rough surface by chemical compounds with low surface energy (Ref 11-13). Several methods, such as lithography, hydrothermal, chemical, and sol-gel, are used to create an artificial hydrophobic surface on metallic substrates (Ref 11-13). However, these methods are very expensive and at times, complicated. Therefore, electrodeposition can be considered as an effective process for the fabrication of hydrophobic surfaces (Ref 11, 14). It would be interesting to check the hydrophobicity of the electrodeposited Zn coating. However, no elaborate analysis has been carried out on the hydrophobic properties of the DC and PC deposition of pure Zn coating developed from the sulfate bath at various current densities.

The current work focuses on the effect of current densities (10, 30, and 60 mA/cm²) on morphological characteristics and corrosion properties of the electrodeposited Zn coatings prepared using the DC and PC deposition techniques. In addition, an elaborate discussion on the hydrophobic behavior of the developed Zn coatings has been carried out. Moreover, the comparative analysis of the electrodeposited Zn coatings and hot-dip galvanized (GI) steel based on coating structure and corrosion property has been successfully elaborated.

2. Experimental Procedure

Interstitial-free (IF) steel with the dimensions of 25 × 25 × 2 mm³ was used as substrate material for the electrodeposition process. The chemical composition of the

IF steel obtained by the optical emission spectrometry (Spectro Maxx) is shown in Table 1. Prior to the electrodeposition process, each steel sample was mechanically polished with silicon carbide (SiC) emery papers up to 2000 grit size. The samples were cleaned with methanol using an ultrasonic cleaning process for 10 min. Finally, the steel samples were rinsed in deionized water and dried by a hot-air blower. For electrodeposition, one side of the steel sample was covered with nail paint, while the other side of the sample was subjected to deposition.

After completion of sample preparation, the steel samples were immediately dipped into the prepared electrolyte solution for the prevention of the oxide layer formed on the polished surface. In the deposition process, the IF steel and 99% of pure Zn were used as cathode and anode, respectively. The area of the anode (Zn strip) was taken to be 2-3 times larger than the cathode material (substrate) to avoid the problem of anodic polarization of Zn, especially at high current densities (Ref 3-5). DC and PC deposition were carried out using a DC machine (Aplab-L6430) and potentiostat (PARASTAT 2273), respectively. In this investigation, a sulfate bath was used for Zn deposition due to its good solution stability, higher current efficiency, and less energy consumption (Ref 14, 15). The optimized chemical composition of the electrolyte bath and operating parameters for the DC and PC deposition are depicted in Table 2.

During the electrolyte bath preparation, the boric acid (H₃BO₃) powder was poured into the deionized water followed by stirring at a speed of 500 rpm for 20 min for complete dispersion of the powder. Then, both Zn sulfate (ZnSO₄·7H₂O) and potassium chloride (KCl) were added to the solution and stirred again for 15 min at 500 rpm. After homogenization of the bath, the pH of the solution was maintained at 9-10 with the addition of the required ammonia hydroxide (NH₃OH). For each electrodeposition test, 300 ml of fresh electrolyte was used. All the electrodeposition tests were carried out at bath temperature of 30 °C at a stirring speed of 300 rpm. After completion of the electrodeposition, the coated sample was rinsed in deionized water and dried.

Moreover, to evaluate the developed electrodeposited coating properties with hot-dip galvanized (GI) coating, a GI-IF steel sample was employed as the reference material. Galvanizing was done by utilizing a typical hot-dip galvanized Zn-Al bath (99% Zn, 0.18% Al). A commercial hot-dip process simulator (HDPS) (M/s. Iwatani Surtec, GmbH, Germany) was used to perform the galvanizing operation. The process parameters used for the hot-dip galvanizing experiment in the current study were already reported in our earlier work (Ref 16).

The electrodeposited as well as the GI steel sheets were mounted transversely using resin powder to characterize the cross-sectional coating structure. The samples were then polished by a silicon carbide paper with a grit size of 2000, followed by cloth polishing with a 1-μ-sized diamond paste. It should be mentioned that methanol was used instead of water

Table 1 Chemical composition of IF steel (wt.%)

C	Si	Mn	P	S	Cr	Mo	Al	Fe
0.042	0.020	0.21	0.016	0.021	0.014	0.007	0.030	Balance

Table 2 Chemical composition of electrolyte bath and deposition conditions

Zinc sulfate, ZnSO ₄ ·7H ₂ O	150 g/l
Potassium chloride, KCl	50 g/l
Boric acid, H ₃ BO ₃	25 g/l
Ammonia hydroxide, NH ₃ OH	2 g/l
Temperature	30 °C
Current density, both DC and PC	10, 30 and 60 mA/cm ²
Plating time	20 min (both DC and PC)
Pulse on-/off-time, ms	60/240 ms
pH	9-10

for polishing Zn-coated samples because Zn is extremely sensitive to water. The coating surface and cross-sectional morphology of the electrodeposited Zn coatings on the steel substrate and the GI steel sheet were characterized by a scanning electron microscope (SEM Nova Nano-450). The chemical composition of the electrodeposited coatings and the GI steel sheet was analyzed by the energy-dispersive spectroscopy (EDS) technique attached to the SEM instrument. The phase analysis of the developed coatings was performed using x-ray diffraction (PANalytical XRD). XRD patterns were obtained using CuK_α radiation (wavelength = 0.154 nm) with a scan rate of 0.01° s⁻¹. In addition, the XRD operations were conducted with an accelerating voltage and filament current of 40 kV and 40 mA, respectively. Moreover, in the present study, the relative texture coefficient (RTC_(hkl)) of all the electrodeposits along with the GI coating was estimated for five crystal planes of Zn by the following formula (Ref 11, 16).

$$RTC_{(hkl)}(\%) = \frac{I_{(hkl)}/I_{0(hkl)}}{\sum (I_{(hkl)}/I_{0(hkl)})} \times 100 \quad (\text{Eq 1})$$

where $I_{(hkl)}$ and $I_{0(hkl)}$ are peak intensities corresponding to the diffracted planes of Zn coatings derived from the XRD results, and the standard peak intensity of Zn derived from the JCPDS data, respectively.

A Vickers hardness tester (Bareiss Prufgeratebau GmbH) was used to measure the microhardness of all the samples, with a load of 10 g and a dwell time of 10 s. The reported hardness value is the average of ten measurements taken from each sample in order to ensure the consistency of measured data.

Atomic force microscope (AFM-AC160TSAR3 model) was used in contact mode with a silicon nitride (SiN) tip to reveal the surface roughness and three-dimensional surface topography images of all the coatings along with the steel substrate. The reported roughness values were the average of ten roughness data determined at different locations of the same coated sample.

Static water contact angles (WCA) of coatings along with steel substrate were measured by VCA Optima Inc., USA, contact angle (CA) goniometer for estimation of the wettability properties at room temperature. The average WCA values were obtained by measuring eight different locations of the same coating surface. The deionized water with a volume of 4 μl was used for the WCA measurements with a dosing rate of 1 μl/s.

The electrochemical impedance spectroscopy (EIS) and Tafel polarization tests were used to analyze the electrochemical behavior of all the coated samples at room temperature in freely aerated 3.5% NaCl solution using a potentiostat

(PARASTAT-3000A). A classical three-electrode cell setup was used for electrochemical tests. In this study, the sample, platinum electrode, and saturated calomel electrode served as working electrode, counter electrode, and reference electrode, respectively. Before each electrochemical measurement, the working electrode was allowed to stabilize in the electrolyte for one hour. This is called open-circuit potential (OCP). The EIS measurements were taken in the frequency ranges of 10⁵-10⁻² Hz with a signal perturbation amplitude of ± 10 mV. Similarly, Tafel polarization was carried out at the potential range of - 250 to + 250 mV with respect to OCP with a scan rate of 0.166 mV/s. The corrosion rate was measured by using Faraday's law (ASTM G102) (Ref 17):

$$\text{Corrosion rate (mm/y)} = \frac{i_{\text{corr}} \times 0.00327 \times EW}{\rho} \quad (\text{Eq 2})$$

where i_{corr} is the corrosion current density (μA/cm²), EW is the equivalent weight and ρ is the density of the element (g/cm³). The morphology of the corroded surface of all the coatings along with the substrate was characterized by SEM. In addition, after the Tafel polarization tests, the corroded bulk samples were directly subjected to the Fourier transforms infrared spectroscopy (FTIR, PerkinElmer Spectrum 2 IR spectrometer) for phase analysis of the corrosion products.

In the current investigation, DC deposition at the current densities of 10, 30, and 60 mA/cm² are referred to as DC 10, DC 30, and DC 60, respectively, as well as PC deposition at the current densities of 10, 30, and 60 mA/cm² are referred to as PC 10, PC 30, and PC 60 mA/cm², respectively.

3. Results and Discussion

3.1 Substrate Characterization

Figure 1(a) and (b) shows the SEM (SE) micrograph and XRD pattern of the IF steel. The microstructure of steel substrate is mainly comprised of ferrite grains (Fig. 1a) due to very low carbon content (0.042 wt.%) (Table 1). Moreover, the XRD pattern (Fig. 1b) of the steel substrate also confirms the presence of crystalline BCC structure of α-ferrite phase with predominant planes of (110), (200), and (211).

3.2 XRD Analysis of Coatings

XRD patterns of the GI steel, as well as the DC- and PC-deposited coatings, are shown in Fig. 2(a). These XRD patterns reveal the presence of crystalline hexagonal (hcp) structure of pure Zn phase with crystal planes of (0002), (10 $\bar{1}$ 0), (10 $\bar{1}$ 1), (10 $\bar{1}$ 2), and (11 $\bar{2}$ 0) at respective positions of 36.5, 39.1, 43.4, 54.5, and 70.5°, respectively. The XRD pattern of pure Zn has been confirmed by the JCPDS card no.1930909. This corroborates well with the earlier investigation (Ref 16). Figure 2(a) also shows the difference in the relative peak intensities of the XRD patterns of all the coatings. To further understand the variations in the relative peak intensities of all the coatings, the RTC values have been calculated and are reported in Table 3. It can be shown from Table 3 that all of the DC deposits have the highest RTC value for (10 $\bar{1}$ 1) crystal plane. This suggests that the growth of the DC-deposited Zn coatings would be more favorable on (10 $\bar{1}$ 1) crystal plane. However, the predominance of mixed texture corresponding to (10 $\bar{1}$ 1/0002) planes could be

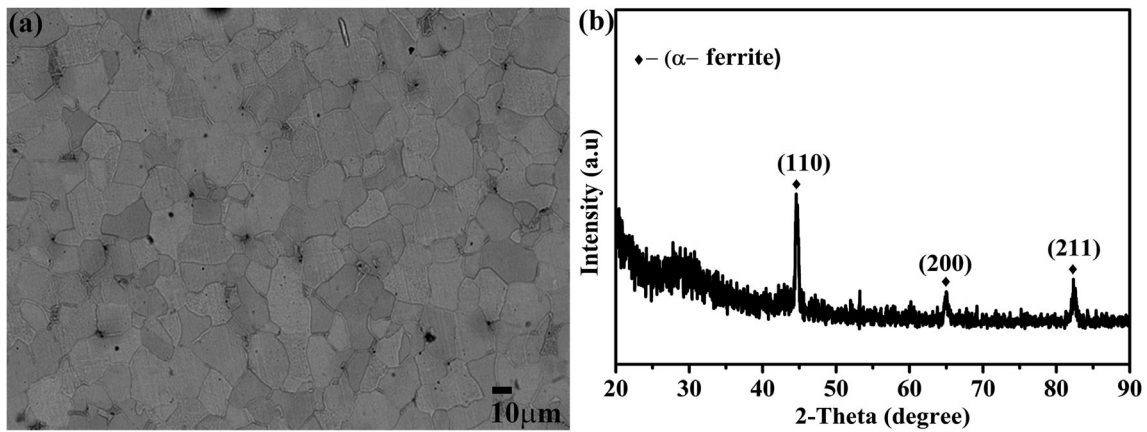


Fig. 1 (a) SEM (SE) micrograph and (b) XRD pattern of the IF steel substrate

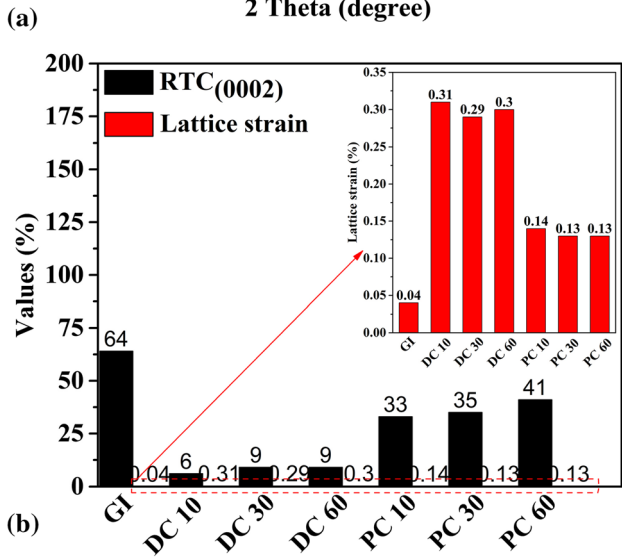
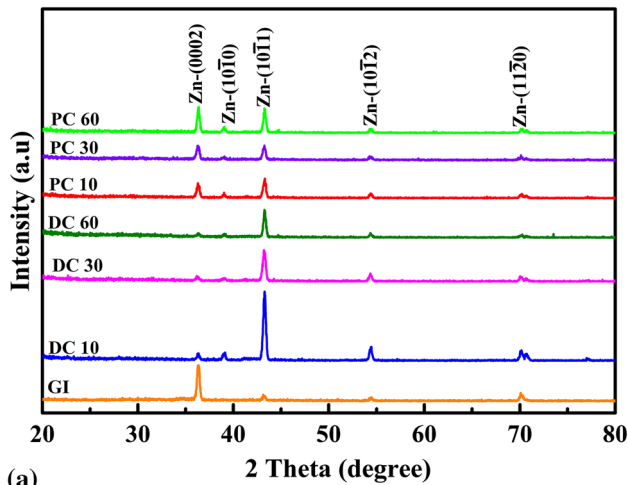


Fig. 2 (a) XRD patterns of all the developed coatings. (b) RTC and lattice strain (%) of DC- and PC-deposited coatings with respect to current densities (10, 30, and 60 mA/cm²) as well as GI coating

seen in all the PC deposits (Table 3). This implies that the crystal growth of the PC-deposited Zn coatings was predominant in the (10 $\bar{1}$ 1) and (0002) planes. Different crystal planes have different electrochemical activities, resulting in different growth rates for each crystal plane. According to the literature

Table 3 The calculated relative texture coefficient (RTC) values from the XRD results

Sample	(0002)	(10 $\bar{1}$ 0)	(10 $\bar{1}$ 1)	(10 $\bar{1}$ 2)	(11 $\bar{2}$ 0)
GI	64	2	12	6	16
DC 10	6	6	63	15	10
DC 30	9	6	59	15	11
DC 60	9	9	65	10	7
PC 10	33	11	39	9	8
PC 30	35	10	36	9	10
PC 60	41	7	40	6	6

(Ref 16, 18), it has been shown that (0002) is the atomically dense plane in Zn. It is interesting to note that in the PC deposition process, 33-41% of the coating is oriented parallel to the (0002) crystal plane as compared to 6-9% in the DC deposition process (Table 3). This indicates that the PC-deposited coatings are more atomically dense than the DC-deposited coating since the growth of coated surface of the DC deposits occurs on (10 $\bar{1}$ 1) crystal plane. As a result, the dominance of the (0002) crystal plane in the PC deposits indicates compact coating morphology and strong interfacial bonding between the substrate and coating (Ref 16, 18). Furthermore, when the deposition current density is increased from 10 to 60 mA/cm², the RTC values for the (0002) crystal plane of the PC deposits increase significantly. However, this is not the case with the DC deposits (Table 3). This indicates that for higher pulse current, the most atomically dense (0002) crystal plane is preferred. In the DC deposits, however, the RTC value for the atomically dense (0002) crystal plane is very low because of the predominance of the (10 $\bar{1}$ 1) crystal plane (Table 3).

In the GI steel, the (0002) crystal plane has the highest RTC value (64%) compared to all the other electrodeposited coatings (Table 3). This suggests that the highest atomically dense (0002) crystal plane of the GI coating has a higher surface atom binding energy, as well as strong interfacial bonding.

Furthermore, the lattice strains ($\delta\%$) for all the coatings have been determined using the following formula (Ref 11, 16) with respect to the (0002) crystal plane:

$$\delta\% = \left(\frac{(d_n(0002) - d_0(0002))}{d_n(0002)} \right) \times 100 \quad (\text{Eq 3})$$

where $d_{(0002)}$ and $d_{(0002)}$ represent the lattice spacings of the (0002) crystal plane of the Zn substrate (unstrained) and the developed Zn coatings (strained), respectively. Figure 2(b) shows the variation in RTC and lattice strains developed on all coatings. Among all the coatings, a higher RTC value for the GI coating corresponds to a lower strain $\epsilon_{(0002)}$, indicating that the atomically dense (0002) crystal orientation is significantly favored over other crystal orientations. Moreover, it has also been demonstrated that the (0002) crystal plane can accommodate less strain than other Zn crystal planes (Ref 16, 18). This suggests that the GI coating is mechanically stronger than other developed coatings. However, the PC deposits have lower strains than the DC deposits due to the dominance of the atomically dense (0002) crystal plane (Fig. 2b).

3.3 Microstructural and Compositional Analysis

It can be observed that the coating surface of the GI coating (Fig. 3a) has compact and uniform morphology. The EDS elemental mapping corresponding to the GI steel as shown by rectangle region in Fig. 3(a) reveals a Zn-rich phase throughout the coated surface (Fig. 3b). Pure Zn nature has been also confirmed by XRD results (Fig. 2). Similarly, the cross-sectional micrograph of the GI coating is shown in Fig. 3(c), and it can be observed that the coating has good adherence to the substrate without the presence of pores. The coating thickness is indicated by a double arrowhead (Fig. 3c). The average thickness of Zn coating in GI is $21.70 \mu\text{m}$. Similarly, the elemental mapping corresponding to the cross-sectional GI coating (as shown by rectangle region in Fig. 3c) reveals the presence of Zn throughout the coating cross-section without the presence of Fe (Fig. 3d). This is obvious in the GI coating. Moreover, a very thin Al-rich layer as inhibition layer is present at the substrate–coating interface. This prevents the diffusion of Fe into Zn coating (Fig. 3d) (Ref 1, 2).

Figure 4(a) shows the top surface morphology of the PC-deposited coating obtained at 60 mA/cm^2 . The uniform distribution of finer Zn crystals throughout the coating surface can be

observed. The elemental mapping of the coated surface (as shown by rectangle region in Fig. 4(a)) reveals the presence of a Zn-rich phase throughout the surface (Fig. 4b). Similarly, Fig. 4(c) displays the coating cross-section of Zn deposit prepared at 60 mA/cm^2 . The coating cross-section morphology shows good adherence to the substrate with an average thickness of $21.55 \mu\text{m}$. The coating thickness region is indicated by a double arrowhead in Fig. 4(c). Furthermore, the elemental mapping of Zn also reveals its uniform distribution in the coating with negligible Fe in the coating (Fig. 4d).

Figure 5 shows the top surface morphologies of the DC- and PC-deposited coatings obtained at various current densities of 10, 30, and 60 mA/cm^2 . Uniform distribution of Zn crystals can be observed throughout the coating surface. ImageJ analysis software has been used to estimate the average grain size of the deposited coatings at each current density. The average grain sizes of the DC-deposited coatings at 10, 30, and 60 mA/cm^2 are calculated to be 5.95 ± 0.65 , 5.80 ± 0.44 , and $5.73 \pm 0.041 \mu\text{m}$, respectively. Similarly, the average grain sizes of the PC-deposited coatings at 10, 30, and 60 mA/cm^2 are 4.20 ± 0.30 , 4.01 ± 0.33 , and $3.89 \pm 0.45 \mu\text{m}$, respectively. Hence, it can be realized that the average grain size of the coatings prepared using the PC deposition process is slightly finer as compared to the DC-deposited coatings at each current density. Higher electrode over-potential results in higher pulse peak current and accompanying increase in nucleation rate on the cathode electrode surface, leading to inhibition of crystal growth (Ref 4, 19). Therefore, it can be concluded that the presence of the preferred (0002) crystal plane in the PC deposits has a significant influence on the grain size as well as the compactness of the electrodeposited coating.

In addition, it can also be observed that the surface morphologies of the DC and PC deposits have changed slightly from coarser to finer with an increase in current density from 10 to 60 mA/cm^2 (Fig. 5a-f). This attributes to the higher nucleation rate with higher current density, leading to grain refining (Fig. 5). A similar trend has also been reported by Tozar et al. (Ref 20) and Ghaziof et al. (Ref 21) for the Zn-Ni coating.

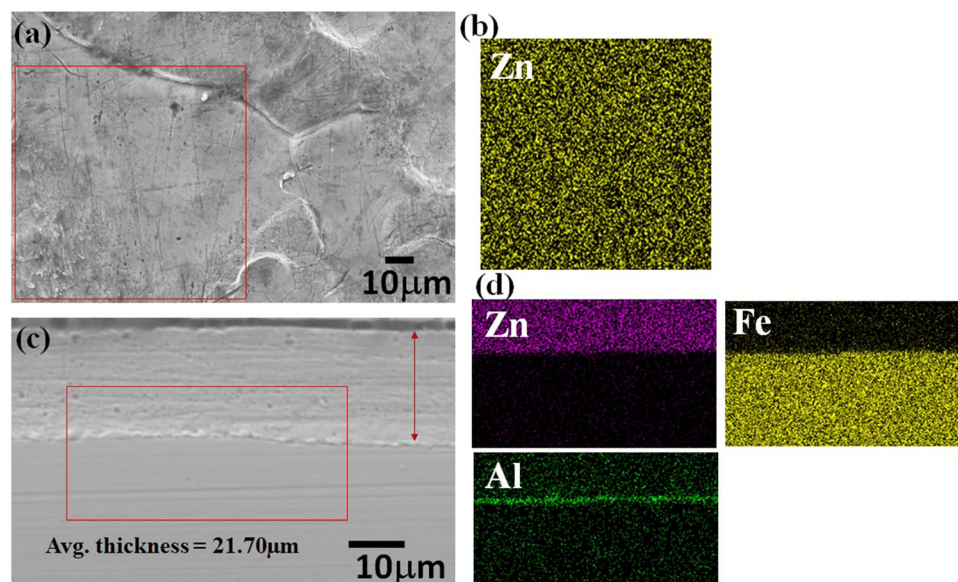


Fig. 3 (a) SEM (SE) micrograph of the GI coating surface and (b) corresponding area elemental mapping of Zn. (c) Coating cross-section of the GI steel and (d) corresponding elemental mapping of Zn, Fe, and Al

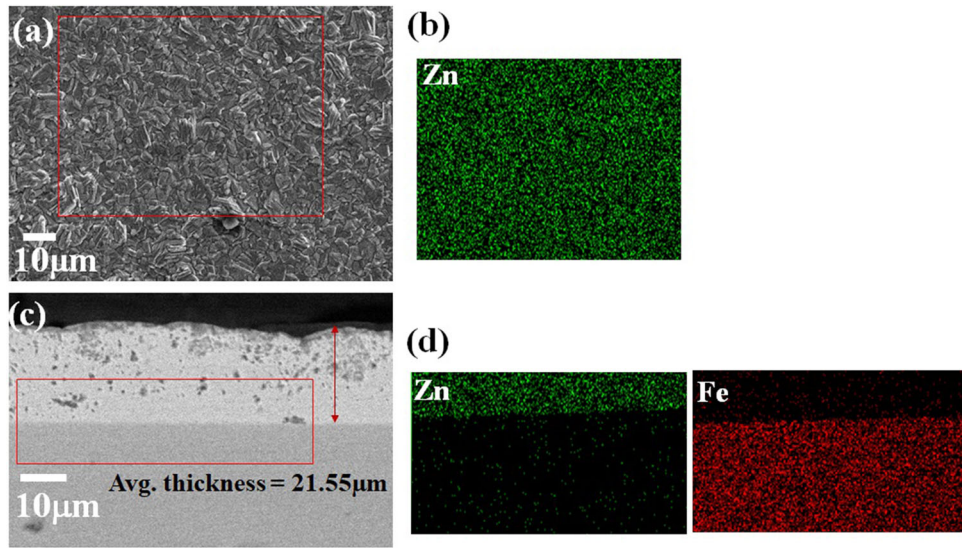


Fig. 4 (a) SEM (SE) micrograph of the PC coating surface prepared at 60 mA/cm^2 and (b) corresponding area elemental mapping of Zn. (c) Cross-section of the PC coating prepared at 60 mA/cm^2 and (d) corresponding elemental mapping of Zn and Fe

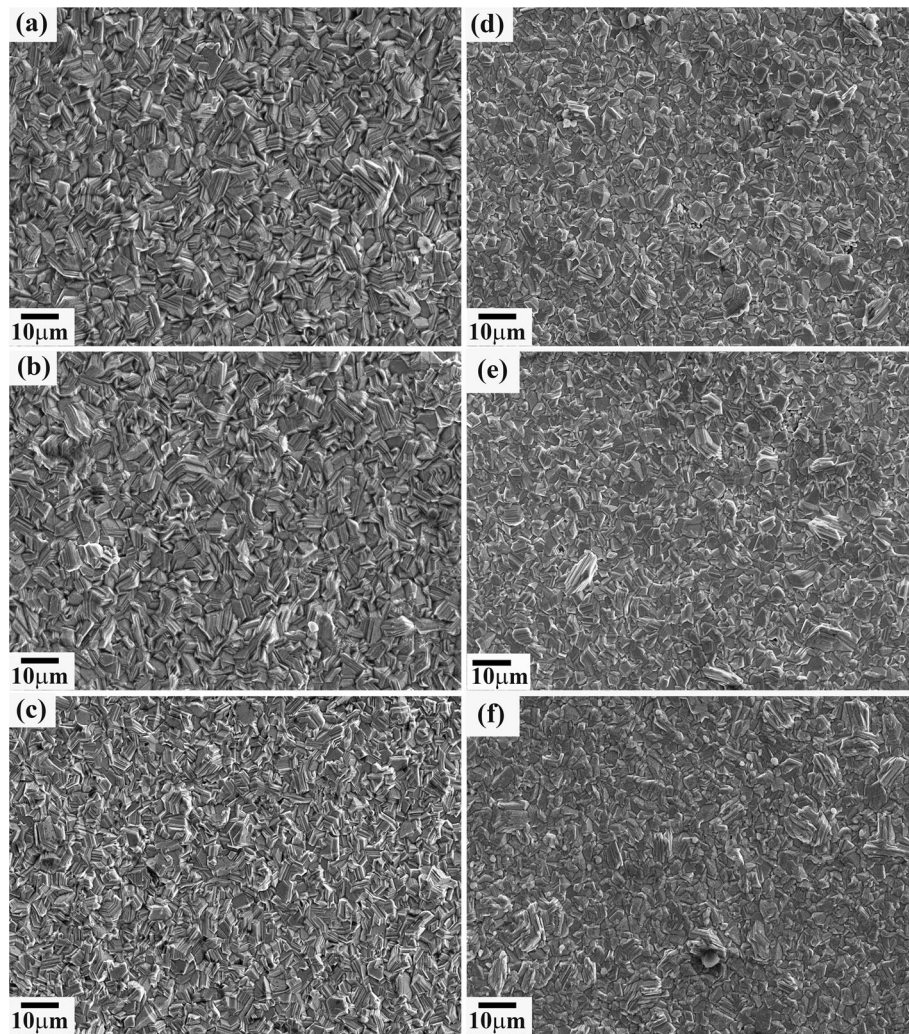


Fig. 5 SEM (SE) top surface micrographs of Zn coating prepared by DC deposition method at (a) 10, (b) 30 and (c) 60 mA/cm^2 as well as PC deposition method at (d) 10, (e) 30 and (f) 60 mA/cm^2 .

It is also worth mentioning that the coating morphologies of all the PC deposits show a finer and compact structure as compared to the DC deposits. In the DC deposition method, constant current density allows more time for the double layer to get charged and stabilized. As a result, Zn ions could migrate to the most stable position for favorable grain growth. In the PC deposition method, the double layer does not have enough time to get fully charged during the on-time (60 ms). It also discharges during the off-time (240 ms). As soon as one pulse cycle is completed, the next pulse arrives very quickly, resulting in very thin pulse diffusion layers making transportation/diffusion of migrating ions from the solution to the steel substrate difficult. Hence, insufficient time is available for the electrical double layer at the substrate and coating interface for charging and discharging during pulse on- and off-time, respectively (Ref 4, 22, 23). This would control the coating growth rate with enhanced nucleation rate, resulting in finer and compact coating in the PC deposits.

Figure 6(a-f) shows the SEM (BSE) micrographs of the cross-sectional coatings obtained from both the DC and PC deposition techniques on the IF steel at various current densities (10, 30, and 60 mA/cm²). On the SEM micrographs (Fig. 6a-f), the coating thickness is indicated by a double arrowhead. The average thickness of the DC deposited coatings is higher than that of the PC-deposited coatings at each applied current density despite the fact that the deposition time (20 min) is the same for all DC- and PC-deposited coatings (Fig. 6a-f). The DC deposition process is continuous since the applied current density is constant leading to thicker coating, whereas the PC deposition process is discontinuous because of the on- and off-time pulse cycle producing thinner coating. In addition, the thickness of the coating increases with an increase in current density for both the DC and PC depositions (Fig. 6a-f). It has been documented that the amount of substance that deposits on the electrode surface during the electrolysis process is directly related to the amount of charge that passes through the cell (Ref 4, 24). This suggests that a higher applied current density (from 10 to 60 mA/cm²) results in more deposition. Furthermore, Fig. 6(a-f) shows that all of the coatings have pores (as shown by arrow marks). When comparing DC and PC deposits, thorough observation reveals that the DC deposits have a

significantly larger pores, and as the coating thickens, making it porous and loosely bonded (Fig. 6a-c). However, while small pores can be seen on the coating cross-sections in the PC deposits (Fig. 6d-f), the coating is more compact, and the visible pores are not deep.

3.4 Surface Roughness and Microhardness Study

Figure 7 shows the 3D AFM topographic images of the GI coating as well as the DC- and PC-deposited coatings along with the steel substrate. The coatings obtained from the DC deposits (Fig. 7c-e) look coarser as compared to the PC deposits (Fig. 7f-h) at each current density of 10, 30, and 60 mA/cm². The average roughness (R_a) values of the polished steel substrate and GI coating have been measured to be 4 and 37 nm, respectively (Fig. 7a and b). However, the coatings obtained from the DC process at 10, 30, and 60 mA/cm² show the average R_a values of 111, 110, and 112 nm, respectively (Fig. 7c-e). Similarly, the average R_a values of the PC-deposited coatings obtained at 10, 30, and 60 mA/cm² are 112, 113, and 115 nm, respectively (Fig. 7f-h). By comparing the R_a values of the coatings obtained from the DC and PC deposits, the PC-deposited coatings show comparatively little higher R_a values than that of the DC deposits. This can also be verified from the morphologies of the coatings observed by AFM topography images. Moreover, the values of the average maximum height of roughness (R_z) of the PC deposits at 10, 30, and 60 mA/cm² are 615, 656, and 698 nm, respectively. Similarly, the average R_z values of the DC deposits at 10, 30, and 60 mA/cm² are 610, 580, and 619 nm, respectively. The higher roughness in the PC-deposited coatings as compared to the DC deposits has been observed in spite of finer and compact morphology in the formers. The higher roughness in the electrodeposited coatings as compared to the GI coating is obvious since the deposition is based on the bombardment of Zn ions against the cathode at different deposition parameters, like solution nature, deposition current density, nucleation rate, etc. (Ref 3-5).

In order to observe the symmetry of the coating morphology, the values of skew roughness (R_{sk}) of all the electrodeposits along with the substrate and GI coating are presented in

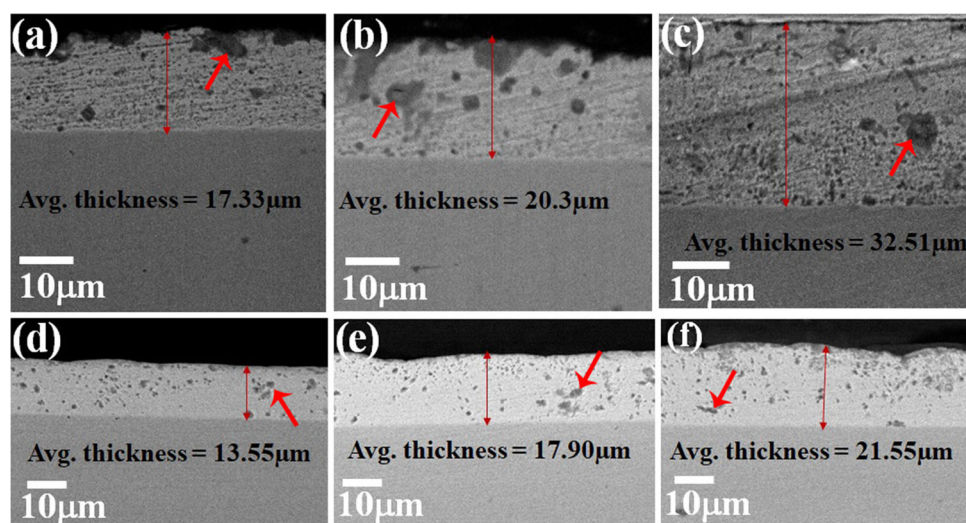


Fig. 6 SEM (BSE) cross-sectional micrographs of Zn coating prepared by DC deposition method at (a) 10, (b) 30 and (c) 60 mA/cm² as well as PC deposition method at (d) 10, (e) 30, and (f) 60 mA/cm².

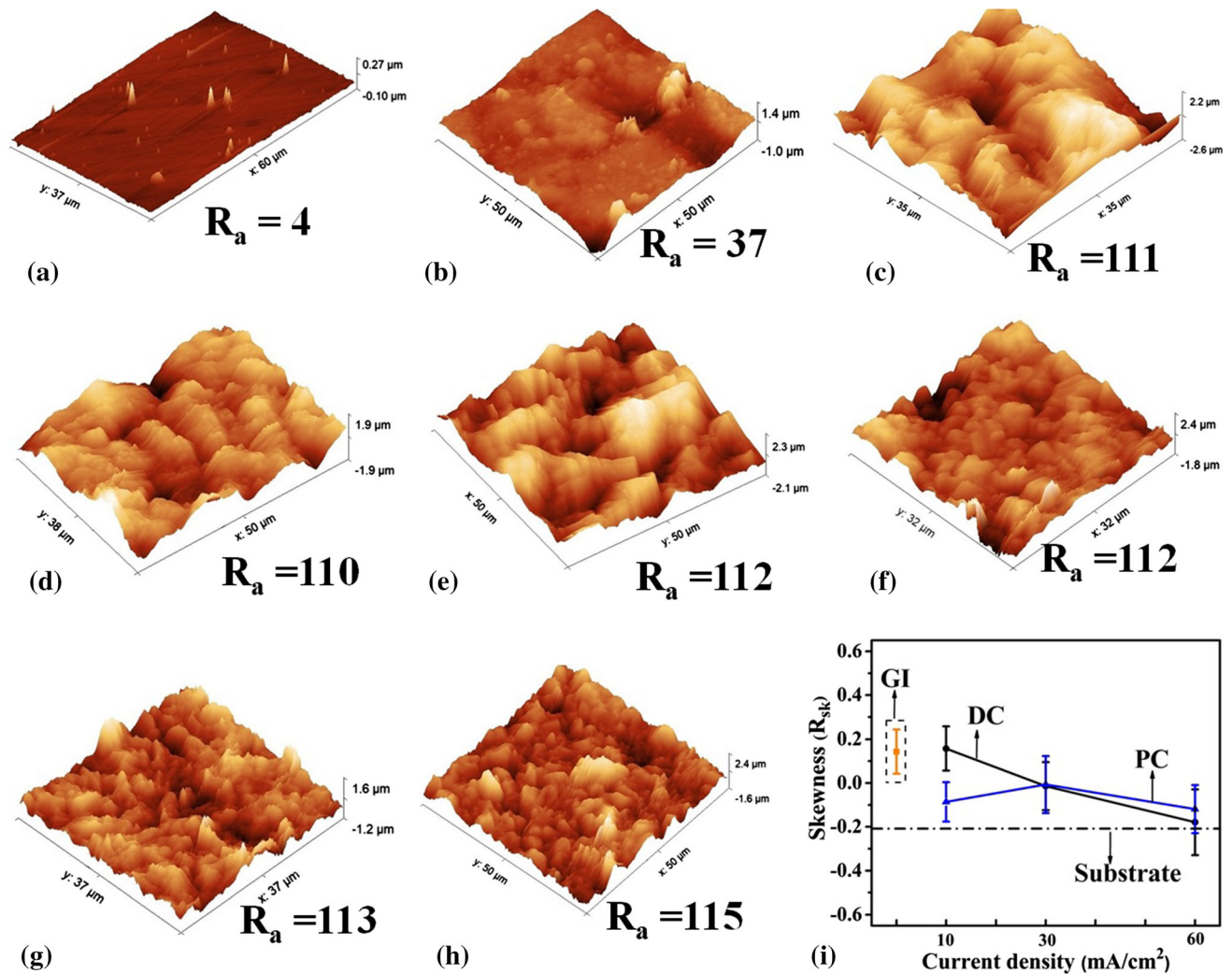


Fig. 7 3D AFM topographic images with surface roughness (R_a in nm) of (a) substrate, (b) GI coating and DC coatings prepared at (c) 10, (d) 30, and (e) 60 mA/cm², as well as PC coatings prepared at (f) 10, (g) 30, and (h) 60 mA/cm². (i) Variation of skewness with current density

Fig. 7(i). The GI coating shows the R_{sk} value of 0.143, whereas the substrate depicts the R_{sk} value of -0.2 . The obtained R_{sk} values for the DC deposits at 10, 30, and 60 mA/cm² are 0.157, -0.014 , and -0.179 , respectively. Similarly, the R_{sk} values are -0.086 , -0.007 , and -0.119 for the PC deposits prepared at 10, 30, and 60 mA/cm², respectively. Generally, if the skewness value of a specific coating is equal to zero (i.e. $R_{sk} \sim 0$), the coating has perfect symmetry (uniform distribution of grains). This means that the PC-deposited samples have more symmetrical coating morphologies as compared to the DC deposits (Ref 13), as the R_{sk} values for the PC deposits are more near to zero. Moreover, the most non-symmetry morphology of the steel substrate (Fig. 1a) is obvious, as the R_{sk} is farthest to zero value. However, the symmetry of the GI steel is equivalent to some of the DC-deposited samples.

Figure 8 shows the average Vickers microhardness (Hv) values of all the coatings as well as the steel substrate. When compared to the deposited coatings (DC and PC), the GI coating has the highest hardness due to the fact that the dominance of the maximum atomically dense (0002) crystal plane enhancing the coating's compactness and atomic density (Table 3). However, regardless of current density, the hardness

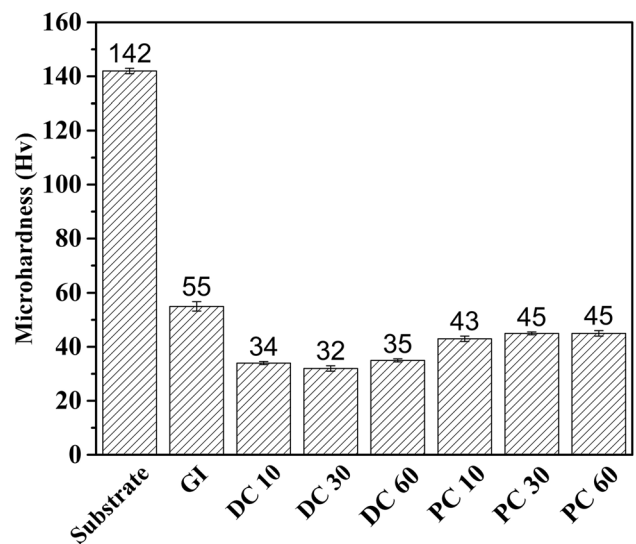


Fig. 8 Average microhardness values of all the developed coatings along with the substrate

values of the PC deposits are higher than those of the DC deposits due to the dominance of the atomically dense (0002) plane in the formers (Table 3). In addition, when compared to the DC deposits, PC deposits contain finer grains with a greater number of grain boundaries, as discussed in Fig. 5, and this impedes dislocation motion and enhances hardness.

3.5 Hydrophobicity

The water contact angle (WCA) values for the coatings and steel substrate are reported in Fig. 9. The polished steel substrate and the GI coating depict WCA of 82 and 100.7°, respectively. According to wettability theory (Ref 11-13), the steel substrate shows hydrophilic behavior, whereas the GI is hydrophobic since the WCA is less than 90° for the substrate and higher than 90° for the GI steel.

However, the deposited coatings obtained from the DC at 10, 30, and 60 mA/cm² show the average WCA values of 99.3, 101.25, and 102.95°, respectively. Similarly, the average WCA values of the PC-deposited coatings obtained at 10, 30, and 60 mA/cm² are 103.50, 105.28, and 107.72°, respectively. Generally, the hydrophobicity of the material can be explained by two hypotheses: one is the Wenzel formulation and the other is the Cassie–Baxter formulation. According to the Wenzel hypothesis, the wettability of a material can be described by the following equation (Ref 11, 25):

$$\cos\theta = r \cos\theta_o \quad (\text{Eq 4})$$

where r , θ , and θ_o are symbolizing the roughness factor, WCA on the coating surfaces, and WCA on the smooth and polished surfaces of the substrate, respectively. According to the Wenzel hypothesis, the WCA should decrease as the roughness of the coated surface increases. However, due to the possibility of air entrapment in the developed coatings, the acquired results in the current investigation contradict. In general, the Wenzel hypothesis is satisfied when there is no air entrapment between the coated surface and the water droplet. Therefore, the Wenzel hypothesis is not valid in this investigation. Similarly, the Cassie–Baxter hypothesis on wettability can be written as follows (Ref 11, 25):

$$\cos\theta = f_s \cos\theta_o - f_a \quad (\text{Eq 5})$$

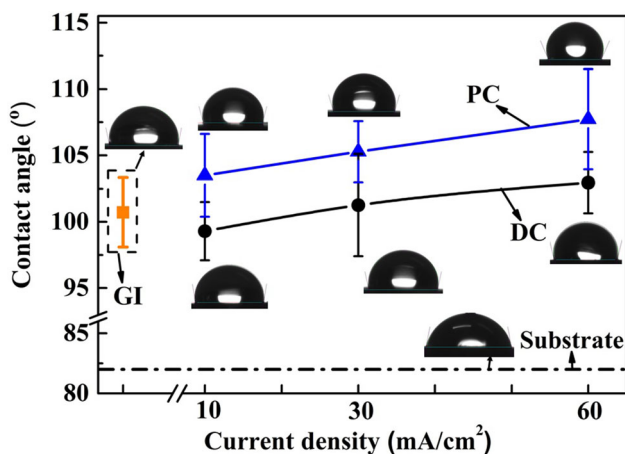


Fig. 9 Variation of water contact angle (WCA) with all the electrodeposited coatings prepared by the DC and PC methods at different current densities (10, 30, and 60 mA/cm²) along with the substrate and GI coating

where θ and θ_o symbolize the WCA on a coating surface composed of solid and air and the WCA on the polished flat steel substrate, respectively. f and $f = (1 - f)$ represent the area fractions of the coating surface in contact with the water droplet and air trapped between the coating surface and water droplet, respectively. The summation of both f and f is equal to unity. This hypothesis tells that the roughness factor is proportional to the hydrophobicity and independent of substrate wettability. Hence, higher surface roughness results in higher air entrapment (higher f value) in between the coating surface and the water droplet. In this investigation, the DC- and PC-deposited samples have higher surface roughness as compared to the steel substrates (Fig. 7). The higher surface roughness results in higher entrapment in the DC-deposited coatings as compared to the substrate impart higher WCA values. Similar trend is also observed in the PC deposits with slightly higher WCA values due to higher surface roughness (Fig. 7). Moreover, the increasing roughness factor with respect to applied current density at both the DC and PC deposition facilitates the WCA values. Therefore, it is concluded that the Cassie–Baxter hypothesis validates the obtained wettability behavior of the synthesized Zn deposits.

3.6 Electrochemical Behavior

Figure 10(a) shows the Tafel polarization curves of the GI steel as well as the DC- and PC-deposited coatings along with the steel substrate in freely aerated 3.5% NaCl solution. Figure 10(b) shows the magnified image of the marked region in Fig. 10(a). The corresponding corrosion potential (E_{corr}), corrosion current density (i_{corr}), anodic and cathodic Tafel slopes ($V_{\text{SCE}}/\text{decade}$), and corrosion rates (mm/y) are shown in Table 4. From the Tafel slopes, it is clear that the corrosion process is guided by the mixed control for the coatings, and oxygen reduction is plausibly the cathodic reaction since the tests are carried out in freely aerated solution. However, the steel substrate is predominantly diffusion-controlled. The E_{corr} and i_{corr} values of the samples were measured from the intercepts on the Tafel slopes by the Tafel extrapolation method.

When compared to the steel substrate, all the Zn-coated steels (GI and electrodeposited steels) exhibit more active (less noble) E_{corr} and are more corrosion-prone (Fig. 10a and Table 4). This demonstrates that in the chloride environment, Zn coatings would give sacrificial protection to the steel. Moreover, all of the coatings' E_{corr} values are less than -0.77 V (Ref 26), which is the protective potential of the steel in the marine environment with respect to the SCE. In addition, it can also be observed that the E_{corr} of the PC-deposited coatings shifts slightly higher potential than that of the DC-deposited coatings at each applied current density (Table 4), suggesting that the PC coatings have a greater nobility than DC coatings. Furthermore, the E_{corr} of the PC-deposited coating prepared at 60 mA/cm² and the GI coating is comparable. Meanwhile, it can also be observed that there is a significant difference in the corrosion rate of the coated samples (Table 4). Among all the coatings, the GI coating and the PC-deposited coating prepared at 60 mA/cm² have shown comparatively lower corrosion rate values of 0.206 and 0.223 mm/y, respectively. The slightly higher corrosion resistance of the GI steel as compared to the PC-deposited coating obtained at 60 mA/cm² can be attributed to the uniform coating structure (Fig. 3) along with a pronounced high atomically dense (0002) crystal plane in terms of

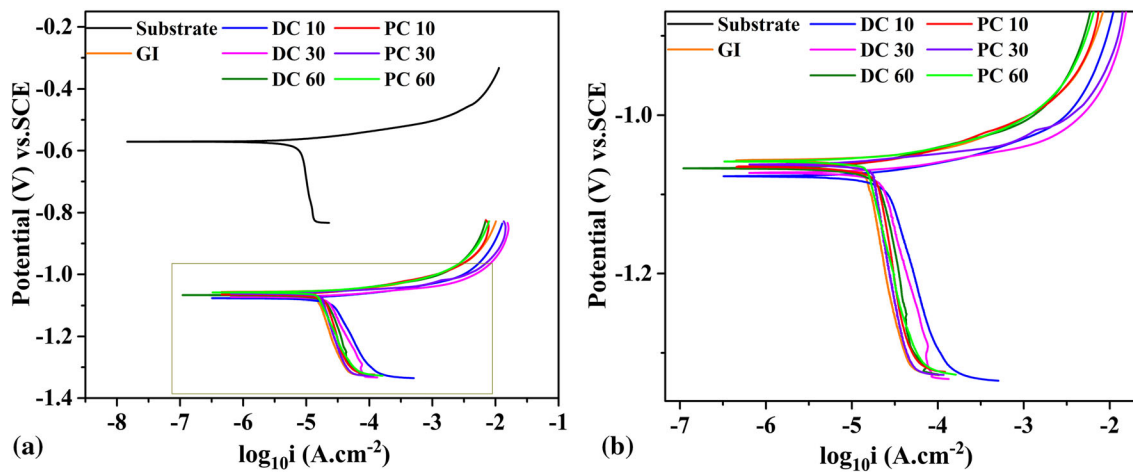


Fig. 10 (a) Tafel polarization plots of all the electrodeposited coatings prepared by DC and PC methods at different current densities (10, 30, and 60 mA/cm²) along with the substrate and GI coating and (b) magnified image of marked region in 10(a)

Table 4 Tafel polarization parameters of all the coatings along with the steel substrate

Sample	E_{corr} V	i_{corr} $\mu\text{A}/\text{cm}^2$	Cathodic slope, $V_{\text{SCE}}/\text{decade}$	Anodic slope, $V_{\text{SCE}}/\text{decade}$	Corrosion rate, mm/y
Substrate	- 0.571	7.80	- 1.125	0.030	0.090
GI	- 1.057	13.80	- 0.569	0.017	0.206
DC 10	- 1.077	24.11	- 0.378	0.029	0.361
DC 30	- 1.072	21.18	- 0.389	0.019	0.317
DC 60	- 1.066	19.36	- 0.562	0.032	0.290
PC 10	- 1.065	18.95	- 0.652	0.036	0.283
PC 30	- 1.062	16.90	- 0.616	0.015	0.253
PC 60	- 1.058	14.93	- 0.440	0.022	0.223

maximum RTC value of (0002) crystal plane (Fig. 2 and Table 3) in the former. In addition, it can also be observed that all the PC-deposited coatings have shown higher corrosion resistance than the DC-deposited coatings at each current density (Table 4). This can be attributed to the compact coating morphologies with less porous nature, and higher RTC values of the (0002) crystal plane, as the higher atomically dense preferred (0002) crystal plane inhibits the ingress of chloride ions (Fig. 2 and 6, and Table 3) (Ref 16). Moreover, it can also be strongly correlated to the comparatively higher contact angle of the PC deposits than the DC-deposited coatings. Higher contact angle results in higher repelling nature of the coating to the electrolyte. Among all the DC- and PC-deposited coatings at various current densities, the lower corrosion rate of the deposited coating obtained at PC-60 mA/cm² can be strongly correlated to lower grain size and higher WCA.

The corrosion rate of the coatings obtained from the DC and PC deposits decreases with an increase in current density (Table 4). This can be attributed to the finer grain size of the coatings since the grain size of coatings decreases with an increase in current density (Fig. 5). The corrosion resistance of deposited coatings as well as GI coating follows in the order of GI > PC 60 > PC 30 > PC 10 > DC 60 > DC 30 > DC 10. The general observation is that the PC improves the corrosion resistance of the electrodeposits as compared to the DC.

To better understand the corrosion behavior of all the coatings along with the substrate at their OCP in a freely

aerated 3.5% NaCl solution, electrochemical impedance spectroscopy (EIS) has been performed. The Nyquist plots of all the coatings and the substrate are shown in Fig. 11(a). The Nyquist plots of all the coatings have two capacitive loops (inset image of Fig. 11(a)): one at the high-frequency range related to the contribution of film resistance and the other at the low-frequency range corresponding to the charge transfer resistance of the double layer (Ref 27, 28). However, a single capacitive loop Nyquist plot could be seen for the substrate, which is related to charge transfer during the corrosion process and double-layer behavior at the electrolyte/metal interface (Fig. 11a). Generally, all the EIS Nyquist plots show a typical capacitive loop. The diameter of the capacitive loop is associated with the resistance to the electrochemical reaction. The larger the diameter of the capacitive loop means greater the corrosion resistance (Ref 16, 28). The diameter of the Nyquist plots of all the coatings in Fig. 11(a) is less than that of the steel substrate, implying that they have inferior corrosion resistance. This has already been demonstrated in the Tafel plots (Fig. 10). In comparison with the PC- and DC-deposited coatings, the GI coating has a larger Nyquist loop diameter at higher and lower frequencies, as seen in the inset image of Fig. 11(a). This implies that all the deposited coatings have a lower charge transfer resistance than the GI coating. Furthermore, at each applied current density, the coatings deposited using the PC have a larger Nyquist loop diameter at higher and lower frequencies than those deposited using DC, indicating that the

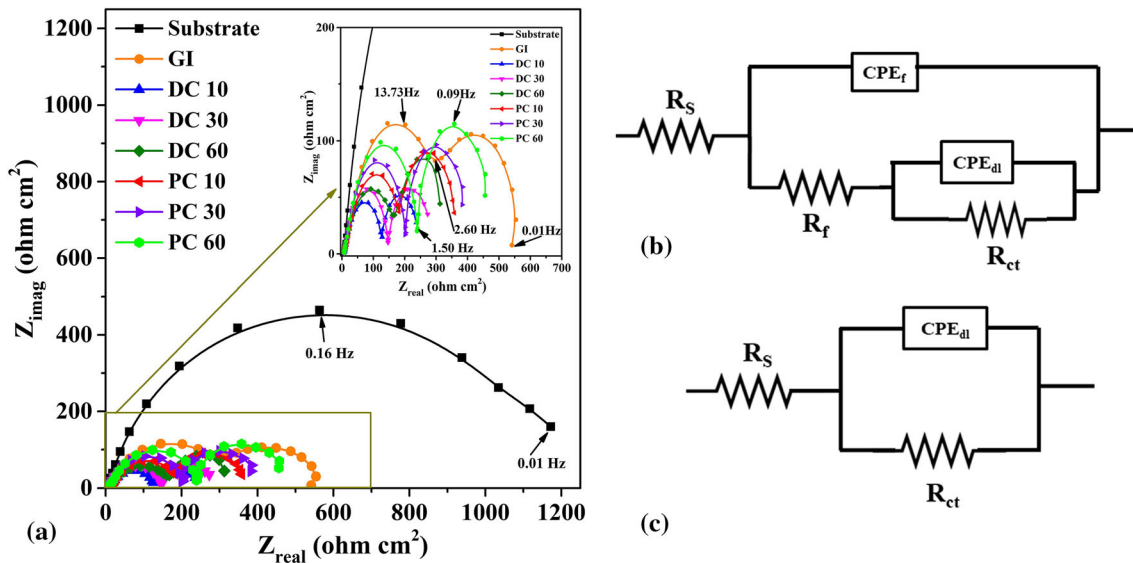


Fig. 11 (a) EIS Nyquist plots of all the electrodeposited coatings prepared by DC and PC methods at different current densities (10, 30, and 60 mA/cm²) along with the substrate and GI coating. Electrochemical equivalent circuit of (b) coated steels and (c) steel substrate

PC deposits have better corrosion resistance than the DC deposits at each applied current density.

The equivalent circuits of R_s (CPE_f (R_f (CPE_{dl} R_{ct}))) and R_s (CPE_{dl} R_{ct}) have been employed in this investigation to extract the EIS data of the coatings and the substrate, respectively, as shown in Fig. 11(b) and (c). In those models, R_s is the solution resistance, CPE_f and R_f represent the capacitance (coating/film/electrolyte interface) and film resistance of the coating, respectively, CPE_{dl} is the electrical double-layer capacitance at the metal/coating/electrolyte interface, and R_{ct} is the charge transfer resistance. Moreover, the goodness of fitting has been assessed with the Chi-square (χ^2) value, which is in the order of 10^{-3} for all the samples. The coating is considered to be porous and reflects a non-ideal behavior in the proposed equivalent circuits for coatings, as indicated by the constant phase element (CPE). The impedance of Z_{CPE_f} and $Z_{CPE_{dl}}$ is given as follows (Ref 27, 28):

$$Z_{CPE_f} = [Y_{of}(j\omega)^{nf}]^{-1} \quad (\text{Eq 6})$$

$$Z_{CPE_{dl}} = [Y_{odl}(j\omega)^{ndl}]^{-1} \quad (\text{Eq 7})$$

where Y_{of} and Y_{odl} are the proportionality constants having dimensions of ($\Omega^{-1} \text{s}^n \text{cm}^{-2}$), j is the imaginary unit ($j^2 = -1$), ω is the angular frequency ($\omega = 2\pi f$, f = frequency) and n is the CPE exponent. As shown in Table 5, all of the samples have 'n' value less than one, indicating that inhomogeneity, defects, and roughness in the sample surface cause deviations from ideal capacitance behavior. In general, when $n = 1, 0,$ and 0.5 represent the ideal capacitor, simple resistor, and Warburg impedance, respectively. However, the Y_0 parameters (Y_{of} and Y_{odl}) are not the actual capacitance, and the effective capacitance of film (CPE_f) and double layer (CPE_{dl}) could be calculated using Brug's equation using the CPE parameter Y_0 as follows (Ref 27, 28):

$$CPE_{dl} = (Y_{odl})^{\frac{1}{n}} \left(\frac{1}{R_s} + \frac{1}{R_c} \right)^{\frac{n-1}{n}} \quad (\text{Eq 8})$$

$$CPE_f = (Y_{of})^{\frac{1}{n}} (R_f)^{\frac{1-n}{n}} \quad (\text{Eq 9})$$

Table 5 shows that Y_0 values are typically inversely related to total polarization resistance ($R_{PR} = R_f + R_{ct}$) values for all coated samples with some deviations, which could be attributed to the porous nature of the coating microstructure (Fig. 6). However, the steel substrate has the lowest Y_0 value due to its more uniform surface and lack of microstructure complexity since only ferrite grains are present. Moreover, the Y_0 values of all the coatings are higher than the steel substrate, implying that the coatings have a lower corrosion resistance (Table 5).

The surface morphologies of all the coatings along with the steel substrate after the Tafel polarization test in freely aerated 3.5% NaCl solution are shown in Fig. 12(a-h). The corroded surface of the IF steel (Fig. 12a) shows uniform corrosion with the formation of patchy oxides. This type of morphology is commonly observed in IF steels, as previously reported by Singh et al. (Ref 29). From Fig. 12(b-h), it can be observed that the corroded surfaces of all the coatings show the distribution of white corrosion products throughout the surface, possibly zinc oxide (ZnO), zinc hydroxide (Zn(OH)₂), and zinc hydroxylchloride (4Zn(OH)₂.ZnCl₂) (Ref 16, 30). The presence of these phases could be confirmed using FTIR analysis (Fig. 13).

Among all the coatings, the GI coating surface shows less corrosion damage with some localized cracks (as shown by arrowhead in Fig. 12(b)) on the coating surface due to the maximum RTC value of (0002) crystal plane (Table 3), which inhibits the ingress of electrolyte ions into the coating and hence reduces coating damage. In the corroded surfaces of the DC deposits at 10 and 30 mA/cm², the coating is removed or peeled off at some areas (as shown by arrowheads in Fig. 12c and d). Similarly, the corroded surface of the DC deposit prepared at 60 mA/cm² (Fig. 12e) displays uniform corrosion with minimal coating damage as compared to the coatings made at 10 and 30 mA/cm² (Fig. 12c and d).

On the other hand, the corroded surfaces of the PC deposits prepared at 30 and 60 mA/cm², the corrosion attacks have mainly happened on the grain boundaries rather than on the

Table 5 Electrochemical parameters of all the coatings along with the steel substrate obtained from EIS analysis

Sample	$R_s, \Omega\text{-cm}^2$	$CPE_{fb}, \Omega^{-1}\text{s}^n\text{cm}^{-2}$	$Y_{0fb}, \Omega^{-1}\text{s}^n\text{cm}^{-2}$	$n1$	$R_f, \Omega\text{-cm}^2$	$CPE_{db}, \Omega^{-1}\text{s}^n\text{cm}^{-2}$	$Y_{0db}, \Omega^{-1}\text{s}^n\text{cm}^{-2}$	$n2$	$R_{ct}, \Omega\text{-cm}^2$	$R_{PR} = R_f + R_{ct}, \Omega\text{-cm}^2$	$\chi^2, \text{Chi-squared}$
Substrate	4.2	9.8×10^{-4}	2.9×10^{-3}	0.80	1252	1252	3.4×10^{-3}
GI	4.1	1.6×10^{-4}	5.3×10^{-4}	0.64	400	6.1×10^{-3}	6.5×10^{-3}	0.98	158	558	7.8×10^{-3}
DC 10	7.8	2.2×10^{-4}	6.3×10^{-4}	0.71	134	16×10^{-3}	1.9×10^{-2}	0.93	105	239	5.6×10^{-3}
DC 30	7.4	4.1×10^{-4}	7.0×10^{-4}	0.81	144	16×10^{-3}	2.2×10^{-2}	0.84	141	285	1.0×10^{-3}
DC 60	6.1	3.3×10^{-4}	5.7×10^{-4}	0.80	191	14×10^{-3}	1.4×10^{-2}	0.98	150	341	3.7×10^{-3}
PC 10	8.6	3.6×10^{-5}	1.9×10^{-4}	0.65	224	10×10^{-3}	1.1×10^{-3}	0.98	145	369	1.2×10^{-3}
PC 30	6.7	8.5×10^{-5}	1.8×10^{-4}	0.82	183	6.8×10^{-3}	1.0×10^{-2}	0.85	238	421	1.2×10^{-3}
PC 60	7.5	6.9×10^{-5}	2.0×10^{-4}	0.74	256	8.5×10^{-3}	9.0×10^{-3}	0.98	217	473	6.1×10^{-3}

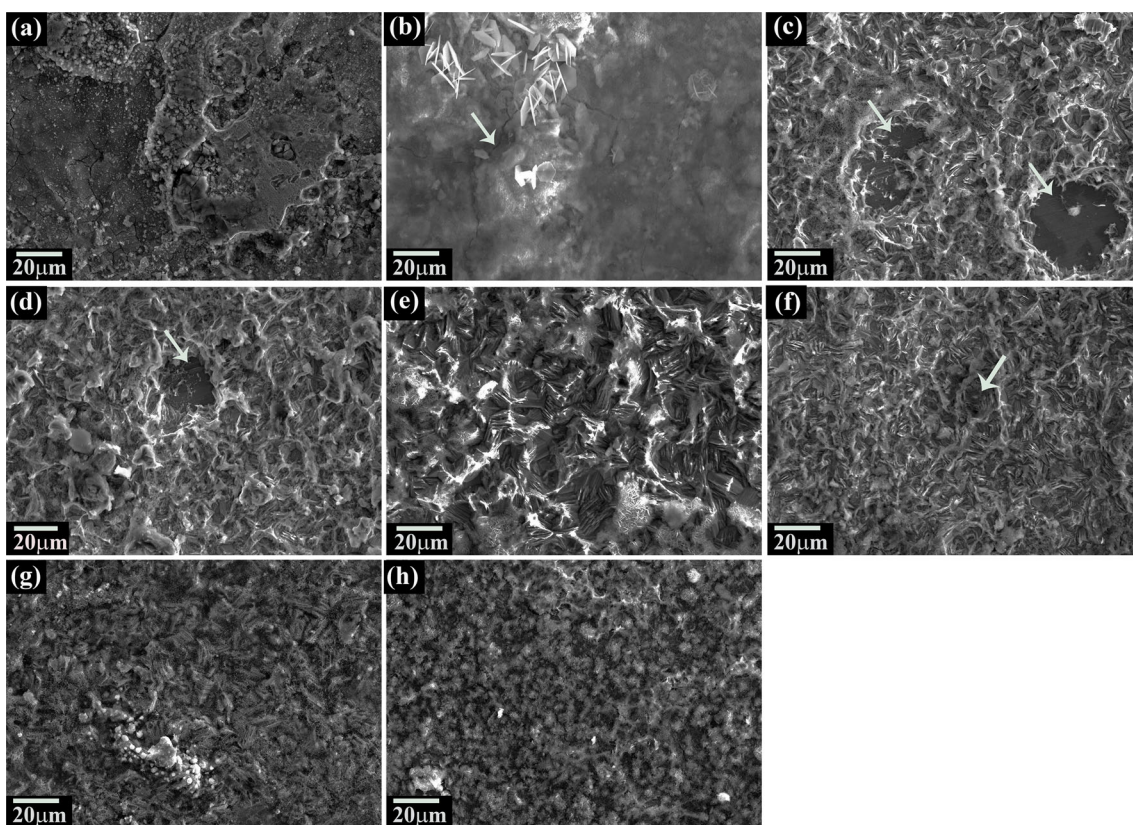


Fig. 12 After corrosion SEM (SE) micrographs of (a) steel substrate, (b) GI coating and DC-deposited coatings at (c) 10, (d) 30, and (e) 60 mA/cm² as well as PC-deposited coatings at (f) 10, (g) 30, and (h) 60 mA/cm².

whole coating surface (Fig. 12g and h). Moreover, the corroded surface of the PC deposit obtained at 10 mA/cm² (Fig. 12f) looks more damaged with deep pits (as shown by arrowhead) as compared to the coatings made at 30 and 60 mA/cm² (Fig. 12g and h). Based on the analysis of the corroded surfaces, the coatings obtained from the PC deposition show uniform corrosion with less coating damage as compared to the DC deposits at each current density (Fig. 12b-h). This attributes to the dominance of the maximum atomically dense (0002) plane in the PC deposits (Table 3), which restricts electrolyte ion ingress into the coating.

All of the corroded samples have been subjected to FTIR after the Tafel polarization tests to identify the corrosion products formed (Fig. 13). Figure 13(a) shows the FTIR spectra of the corroded surface of the steel substrate, demonstrating that the corrosion products are α -FeOOH, γ -FeOOH,

β -FeOOH, and α -Fe₂O₃ (Ref 29). The presence of zinc oxide (ZnO), zinc hydroxide (Zn(OH)₂), zinc hydroxychloride (4Zn(OH)₂.ZnCl₂), and zinc carbonate (ZnCO₃) is confirmed by the FTIR spectra of all the coated samples (Fig. 13b). Zinc hydroxychloride (4Zn(OH)₂.ZnCl₂) is commonly known as simonkolleite (Ref 16, 30). Furthermore, the existence of water molecules is indicated by the broad and intense peak between 3482 and 3451 cm⁻¹. Generally, when the Zn coating is exposed to a freely aerated 3.5% NaCl solution, various reactions occur at the coating–electrolyte interface. Firstly, the dissolution of Zn results in the generation of electrons (Eq 10), which is followed by the generation of hydroxyl ions when the released electrons react with the water molecules (Eq 11) (Ref 16, 30).



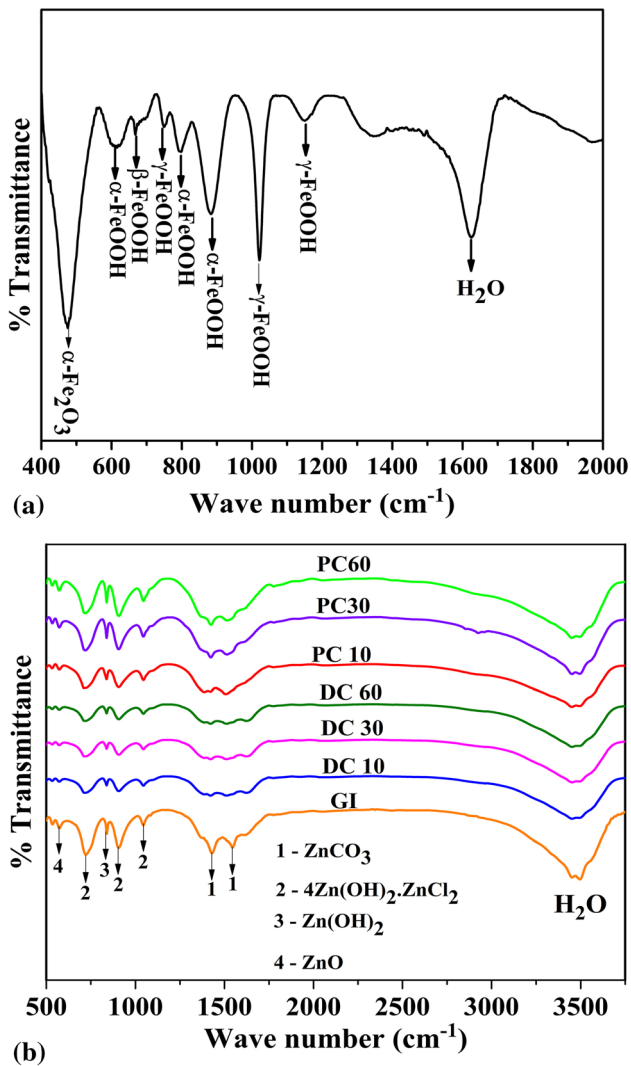
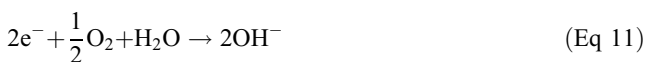


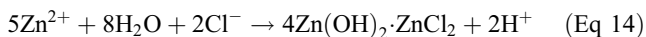
Fig. 13 The FTIR spectra after Tafel polarization in freely aerated 3.5% NaCl solution for (a) steel substrate and (b) developed coatings



Hydroxyls react with Zn ions, and zinc hydroxides could form (Eq 12). These zinc hydroxides disintegrate and form zinc oxides (Eq 13).



However, in the presence of a chloride environment, the following reaction produces simonkolleite (zinc hydroxychloride) (Eq 14).



Furthermore, the corrosion products formed on the coated samples react with the atmospheric CO₂ to form zinc carbonate (ZnCO₃). All of these reactions could be possible since the rust layer on the coatings shows all the reaction products (Fig. 13). Many literatures have reported the influence of phase fraction of simonkolleite in corrosion products on corrosion rate

(Ref 31-33). The phase fraction of the simonkolleite has been shown to rise as the corrosion rate decreases. Simonkolleite is the most compact corrosion product phase as compared to other Zn corrosion products. It can minimize the oxygen reduction rate on the coating surface and slow-down corrosion (Ref 31-33).

The phase fraction of the simonkolleite has been determined using the area of the FTIR peaks in this study. The FTIR spectra of all the coated samples have been normalized, and baseline adjustment has been performed using OriginPro-2015 software before determining the phase fraction. The simonkolleite phase fraction has been calculated by dividing the sum of the area of FTIR peaks pertaining to the simonkolleite phase by the sum of the area of all peaks in the spectra (Ref 16, 33). The phase fraction of the simonkolleite produced on the PC deposits (82.2% at PC 10, 83.3% at PC 30, and 83.10% at PC 60) has been found to be higher than that of the DC deposits (72.5% at DC 10, 75.8% at DC 30, and 77.3% at DC 60), indicating that the PC deposits are more corrosion resistant than the DC deposits (Fig. 10 and Table 4). Moreover, few studies have reported that the fine-grained Zn coating structure is more prone to corrosion due to the higher volume fraction of the grain boundaries (Ref 34). In the present work, the Zn coatings made by the PC show finer grains as compared to the DC (Fig. 5). As a result, the corrosion rate of the PC-deposited samples should have been higher. In contrary, the corrosion resistance of the PC-deposited samples is better than those made by the DC. Hence, the presence of a higher fraction of the simonkolleite phase in the Zn coatings made by the PC serves better corrosion resistance. Moreover, the surface of the Zn coating made by PC generally shows higher surface coverage by the oxide and lesser defects (Fig. 12f-h). Furthermore, the GI coating's simonkolleite phase fraction (84.1%) is identical to that of the PC deposits. Therefore, the GI steel and the PC coated steels show a similar corrosion rate (Fig. 10 and Table 4).

Therefore, compact nature, a predominance of compact (0002) texture, higher WCA, and a higher fraction of protective simonkolleite in the Zn coatings made by the PC deposition impart higher corrosion resistance as compared to the coatings made by the DC method. Moreover, the PC-coated steel at 60 mA/cm² shows corrosion resistance similar to the Zn coatings made by hot-dip galvanization.

4. Conclusions

The Zn coating on IF steel has been successfully formed by both the DC and PC electrodeposition techniques at various current densities of 10, 30, and 60 mA/cm². The coating surface morphologies obtained from the PC deposits are finer and more compact than DC deposits at each current density. Moreover, the current study also reveals the presence of the highest atomically dense (0002) crystal plane in the PC deposits as compared to the DC deposits. In comparison with all the coatings, the GI coating and PC-electrodeposited coating prepared at 60 mA/cm² have the lowest corrosion rate values of 0.206 mm/y and 0.223 mm/y, respectively. Moreover, the highest WCA value of 107.72° for the PC deposit obtained at 60 mA/cm² can be observed. In addition, it has been also observed that all the PC-deposited coatings have shown higher corrosion resistance than the DC-deposited coatings at each

current density because the PC deposits have finer and compact coating morphology along with higher atomically dense of (0002) crystal plane, higher WCA values as well as the higher fraction of simonkolleite phase as compared to the DC deposits.

References

1. A.R. Marder, The Metallurgy of Zinc-Coated Steel, *Prog. Mater. Sci.*, 2000, **45**, p 191–271.
2. S.M.A. Shibli, B.N. Meena, and R. Remya, A Review on Recent Approaches in the Field of Hot-Dip Zinc Galvanizing Process, *Surf. Coat. Technol.*, 2015, **262**, p 210–215.
3. K.K. Maniam and S. Paul, Corrosion Performance of Electrodeposited Zn and Zn Alloy Coatings in Marine Environment, *Corros. Mater. Degrad.*, 2021, **2**, p 163–189.
4. M.S. Chandrasekar and M. Pushpavanam, Pulse and Pulse Reverse Plating—Conceptual, Advantages and Applications, *Electrochim. Acta*, 2008, **53**, p 3313–3322.
5. C.A. Loto, Electrodeposition of Zn from Acid Based Solutions: A Review and Experimental Study, *Asian J. Appl. Sci.*, 2012, **5**(6), p 312–326.
6. F.H. Assaf, S.S. Abd El Rehim, A.S. Mohamed, and A.M. Zaky, Electroplating of Brass from Citrate-Based Alloy Baths, *Indian J. Chem. Technol.*, 1995, **2**(3), p 147–152.
7. C.J. Chen and C.C. Wan, A Study of the Current Efficiency Decrease Accompanying Short Pulse Time for Pulse Plating, *J. Electrochem. Sci.*, 1989, **136**, p 2850–2855.
8. K. Arunsunai Kumar, G. Paruthimal Kalaigann, and V.S. Murali Dharan, Direct and Pulse Current Electrodeposition of Ni–W–TiO₂ Nano-Composite Coatings, *Ceram. Int.*, 2013, **39**, p 2827–2834.
9. T.M. Al-Dhire, H. Zuhailawati, and A.S. Anasyida, Effect of Current Density on Corrosion and Mechanical Properties of Zn–SiC Composite Coating, *Mater. Today: Proc.*, 2019, **17**, p 664–671.
10. J.C. Scully, *The Fundamentals of Corrosion*, 2 edn (Pergamon Press, Oxford, 1990)
11. H.S. Maharana, P.K. Katiyar, and K. Mondal, Structure Dependent Super-Hydrophobic and Corrosion Resistant Behavior of Electrodeposited Ni–MoSe₂–MWCNT Coating, *Appl. Surf. Sci.*, 2019, **478**, p 26–37.
12. C. Li, R. Ma, Y. Du An, X. Fan, and X. Cao. Zhao, One-Step Fabrication of Bionic Superhydrophobic Coating on Galvanized Steel with Excellent Corrosion Resistance, *J. Alloys Compd.*, 2019, **786**, p 272–283.
13. T. Darmanin, E.T. de Givenchy, S. Amigoni, and F. Guittard, Superhydrophobic Surfaces by Electrochemical Processes, *Adv. Mater.*, 2013, **25**, p 1378–1394.
14. F. Azizi and A. Kahoul, Electrodeposition and Corrosion Behavior of Zn–Co Coating Produced from a Sulphate Bath, *Trans. IMF*, 2016, **94**, p 43–48.
15. M.M. Abou-Krishna, A.G. Alshammari, F.H. Assaf, and F.A. El-Sheref, Electrochemical Behavior of Zn–Co–Fe Alloy Electrodeposited from a Sulfate Bath on Various Substrate Materials, *Arabian. J. Chem.*, 2019, **12**, p 3526–3533.
16. H. Kancharla, G.K. Mandal, S.S. Singh, and K. Mondal, Effect of Strip Entry Temperature on the Interfacial Layer and Corrosion Behavior of Galvanized Steel, *Surf. Coat. Technol.*, 2022, **433**, p 128071–128085.
17. ASTM G102-89, e1, *Standard Practice for Calculation of Corrosion Rates and Related Information from Electrochemical Measurements*, (ASTM INTERNATIONAL, West Conshohocken, PA, 2015)
18. H. Asgari, M.R. Toroghinejad, and M.A. Golozar, Effect of Coating Thickness on Modifying the Texture and Corrosion Performance of Hot-Dip Galvanized Coatings, *Curr. Appl. Phys.*, 2009, **9**, p 59–66.
19. M.S. Chandrasekar, S. Srinivasan, and M. Pushpavanam, Structural and Textural Study of Electrodeposited Zinc from Alkaline Non-Cyanide Electrolyte, *J Mater Sci.*, 2010, **45**, p 1160–1169.
20. A. Tozar and I.H. Karahan, Structural and Corrosion Protection Properties of Electrochemically Deposited Nano-Sized Zn–Ni alloy Coatings, *Appl. Surf. Sci.*, 2014, **318**, p 15–23.
21. S. Ghaziof and W. Gao, The Effect of Pulse Electroplating on Zn–Ni Alloy and Zn–Ni–Al₂O₃ Composite Coatings, *J. Alloys Compd.*, 2015, **622**, p 918–924.
22. S. Anwar, Y. Zhang, and F. Khan, Electrochemical Behavior and Analysis of Zn and Zn–Ni Alloy Anti-Corrosive Coatings Deposited from Citrate Baths, *RSC Adv.*, 2018, **8**, p 28861–28873.
23. H.S. Maharana, S. Lakra, S. Pal, and A. Basu, Electrophoretic Deposition of Cu–SiO₂ Coatings by DC and Pulsed DC for Enhanced Surface-Mechanical Properties, *J. Mater. Eng. Perform.*, 2016, **25**, p 327–337.
24. A. Fazazi, M. Ouakki, and M. Cherkaoui, Electrochemical Deposition of Zn on Mild Steel, *Mediterr. J. Chem.*, 2019, **8**, p 30–41.
25. Y. He, W.T. Sun, S.C. Wang, P.A.S. Reed, and F.C. Walsh, An Electrodeposited Ni–P–WS₂ Coating with Combined Super-Hydrophobicity and Self-Lubricating Properties, *Electrochim. Acta*, 2017, **245**, p 872–882.
26. A.W. Peabody, *Peabody's Control of Pipeline Corrosion*, second edn. (NACE International, 2001)
27. J. Shi, J. Ming, D. Wang, and M. Wu, Improved Corrosion Resistance of a new 6% Cr Steel in Simulated Concrete Pore Solution Contaminated by Chlorides, *Corros. Sci.*, 2020, **174**, p 108851.
28. N.Kr. Prasad, A.S. Pathak, S. Kundu, and K. Mondal, Novel Hybrid Sacrificial Anodes Based on High Phosphorus Pig Iron and Zn, *Corros. Sci.*, 2021, **189**, p 109616.
29. G.P. Singh, A.P. Moon, S. Sengupta, G. Deo, S. Sangal, and K. Mondal, Corrosion Behavior of IF Steel in Various Media and its Comparison with Mild Steel, *J. Mater. Eng. Perform.*, 2015, **24**, p 1961–1974.
30. T.E. Graedel, Corrosion Mechanisms for Zinc Exposed to the Atmosphere, *J. Electrochem. Soc.*, 1989, **136**, p 193C–203C.
31. P. Volovitch, T.N. Vu, C. Allély, A. Abdel Aal, and K. Ogle, Understanding Corrosion Via Corrosion Product Characterization: II. Role of Alloying Elements in Improving the Corrosion Resistance of Zn–Al–Mg coatings on Steel, *Corros. Sci.*, 2011, **53**, p 2437–2445.
32. R. Autengruber, G. Luckeneder, and A.W. Hassel, Corrosion of Press-Hardened Galvanized Steel, *Corros. Sci.*, 2012, **63**, p 12–19.
33. H. Kancharla, G.K. Mandal, S.S. Singh, and K. Mondal, Effect of Prior Copper-Coating on the Microstructural Development and Corrosion behavior of Hot-Dip Galvanized Mn Containing High Strength Steel Sheet, *Surf. Coat. Technol.*, 2022, **437**, p 128347.
34. C.C. Lin and C.M. Huang, Zn–Ni Alloy Coatings Electrodeposited by Pulse Current and their Corrosion Behavior, *J Coat. Technol. Res.*, 2006, **3**, p 99–104.

Publisher's Note Springer Nature remains neutral with regard to jurisdictional claims in published maps and institutional affiliations.